Fluctuating zonal flows in the I-mode regime in Alcator C-Mod[a)]

I. Cziegler,[b)] P. H. Diamond,[1] N. Fedorczak,[1] P. Manz,[1] G. R. Tynan,[1] M. Xu,[1]
R. M. Churchill,[2] A. E. Hubbard,[2] B. Lipschultz,[2] J. M. Sierchio,[2] J. L. Terry,[2] and C. Theiler[2]
[1]*Center for Momentum Transport and Flow Organization, University of California, San Diego, La Jolla, California 92093, USA*
[2]*Plasma Science and Fusion Center, Massachusetts Institute of Technology, Cambridge, Massachusetts 02138, USA*

(Received 14 December 2012; accepted 4 March 2013; published online 7 May 2013)

Velocity fields and density fluctuations of edge turbulence are studied in I-mode [F. Ryter *et al.*, Plasma Phys. Controlled Fusion **40**, 725 (1998)] plasmas of the Alcator C-Mod [I. H. Hutchinson *et al.*, Phys. Plasmas **1**, 1511 (1994)] tokamak, which are characterized by a strong thermal transport barrier in the edge while providing little or no barrier to the transport of both bulk and impurity particles. Although previous work showed no clear geodesic-acoustic modes (GAM) on C-Mod, using a newly implemented, gas-puff-imaging based time-delay-estimate velocity inference algorithm, GAM are now shown to be ubiquitous in all I-mode discharges examined to date, with the time histories of the GAM and the I-mode specific [D. Whyte *et al.*, Nucl. Fusion **50**, 105005 (2010)] Weakly Coherent Mode (WCM, $f = 100$–$300\,\mathrm{kHz}$, $\Delta f/f \approx 0.5$, and $k_\theta \approx 1.3\,\mathrm{cm}^{-1}$) closely following each other *through the entire duration of the regime*. Thus, the I-mode presents an example of a plasma state in which zero frequency zonal flows and GAM continuously coexist. Using two-field (density-velocity and radial-poloidal velocity) bispectral methods, the GAM are shown to be coupled to the WCM and to be responsible for its broad frequency structure. The effective nonlinear growth rate of the GAM is estimated, and its comparison to the collisional damping rate seems to suggest a new view on I-mode threshold physics. © *2013 AIP Publishing LLC*. [http://dx.doi.org/10.1063/1.4803914]

I. INTRODUCTION

During the last decade, zonal flows (ZFs) have garnered a considerable amount of attention in the literature of plasma turbulence, due in large part to the role they play in the formation of energy and mass transport barriers.[1–3] Turbulence is now broadly believed to be the dominant source of plasma transport in magnetically confined plasmas, such as tokamaks and other fusion devices, leading to cross-field transport which exceeds the classical or neoclassical predictions often by more than an order of magnitude.[4,5] The key mechanism for the reduction of this turbulent transport process in high-confinement scenarios is the reduction of turbulence by velocity shear.[6,7] Both toroidally and poloidally symmetric ($n = m = 0$) but radially sheared (hence the term "zonal") $\mathbf{E} \times \mathbf{B}$ flows cannot only provide this radial shearing but they can also be nonlinearly driven by the turbulence[8,9] itself thus producing a saturation mechanism inherent to the plasma turbulence.

In toroidal geometry, theory classifies these flows mostly by their temporal characteristics as zero-frequency ZF, often referred to as Rosenbluth–Hinton-modes,[10] usually occurring with a finite but small frequency range, and the geodesic-acoustic modes (GAM)[11] which are distinctly coherent modes at a frequency that is approximately $\omega_{\mathrm{GAM}} = c_s/R$, where c_s is the sound speed and R the major radius of the torus. Generally, the two branches have their specific ranges spatially as well as in a parametric sense. At small values of the safety factor q, GAM are strongly Landau damped,[12] and due to their finite frequency, they are also more susceptible to collisional damping[13] than the ZF. Consequently, GAM are usually not observed in the low q core plasma nor are they usually observed in the high confinement regime (H-mode) where strong mean shear flow reduces turbulence to such a low level that it is no longer able to nonlinearly drive the mode. In the "zonal-flow–drift-wave-turbulence" paradigm of transport regulation, both analytic and numeric studies have given significant roles to both kinds of flows in the physics of phase transitions between confinement regimes. Recent experimental work has directly demonstrated the interaction of mean ZF and GAM with the edge turbulence in L-mode[14] leading up to low-to-high (L-H) confinement transitions,[15] as well as in intermediate regimes.[16,17] The fine details of the nonlinear transfer processes as well as studies of less common confinement regimes are currently in the focus of much experimental research.

Indeed one of the most important recent developments in the physics of the L-H transition has been the detailed characterization of the I-mode.[18–21] This confinement regime was originally reported to appear in the ASDEX-Upgrade tokamak[18] as an intermediate step in the transition to H-mode when the ion $\nabla\mathbf{B} \times \mathbf{B}$ drift was directed away from the active X-point, the poloidal null-point of the last closed flux surface (LCFS). This geometry is usually known as "unfavorable," because ever since the first observation of the H-mode, it has been reported to cause the threshold input power required for an H-mode to be around a factor of two higher than with the opposite ion $\nabla\mathbf{B} \times \mathbf{B}$ direction.[22]

[a)]Paper YI3 5, Bull. Am. Phys. Soc. **57**, 372 (2012).
[b)]Invited speaker; Electronic mail: cziegler@ucsd.edu

Similar improvements of confinement in the pre-H-mode phase were reported on Alcator C-Mod[23] and other tokamaks[24] in this configuration. Of significant interest is the fact that the edge energy and mass transport channels are very clearly separated in the I-regime. The I-mode is characterized by a strong thermal transport barrier in the edge while providing little or no barrier to the transport of either bulk or impurity particles. This allows access to steady state, high performance discharges without explosive edge relaxations or impurity accumulation.

More recently, Alcator C-Mod[25] demonstrated the feasibility of a stationary I-mode,[26] lasting several confinement times and avoiding a transition into a regular H-mode altogether. The regime is still mostly accessed in the "unfavorable" magnetic field configuration and it is identifiable by a number of edge turbulence characteristics, including a weakly coherent mode (WCM) reported to exist in the edge density, temperature, and magnetic field fluctuations[19] at $f = 100$–300 kHz, $\Delta f/f \approx 0.5$, a moderate reduction of turbulence in the mid-range (50–150 kHz)[20,21] of frequencies and an edge localized $\mathbf{E} \times \mathbf{B}$ flow[26] somewhat smaller than that in H-modes. Given that the I-mode features a temperature- but no density-pedestal, the regimes exists at low edge collisionalities, $\nu^* = 0.1 - 1$.

The present paper reports optical measurements of the edge turbulence in the I-mode regime. Using density fluctuations to infer the turbulent velocity field, GAM is found for the first time in Alcator C-Mod to exist in the edge region of all I-mode discharges. To address the issue of turbulence-flow interactions, direct measurements of the density–poloidal-velocity cross-bispectra are studied and the broad frequency structure of the WCM is found to be due to a strong coupling to the GAM. Since the WCM activity is strongly correlated to the I-mode behavior, and due to the known dependence of the GAM damping on collisionality,[13] this observation suggests that the WCM-GAM coupling may play a role in determining the previously reported scalings of I-mode accessibility.[21]

The rest of the paper is organized as follows. Section II describes the most important operating parameters of the plasmas evaluated in this study, as well as the arrangement of the utilized diagnostics and the methods employed for the analysis of their data. Results identifying the main feature of the poloidal velocity spectrum as a GAM are presented in Sec. III, after which some further spatial characteristics are discussed in Sec. IV. Measurements of the nonlinear transfer terms (bispectra) are shown and interpreted in Sec. V. Once nonlinear drive of the GAM is quantified, it is compared to expected damping terms in Sec. VI in a time-resolved sense, followed by a brief summary and discussion of the results in Sec. VII.

II. EXPERIMENTAL SETUP AND METHODS

All the experiments reported in this paper were performed on the Alcator C-Mod tokamak,[25] a compact ($R_0 = 0.68$ m, $a \simeq 0.21$ m) toroidal device with a high magnetic field (up to $B_\phi \leq 8$ T, with a typical $B_\phi = 5.4$ T). The I-modes studied here were produced with plasma currents of $I_p = 0.8 - 1.35$ MA and toroidal magnetic fields of $B_\phi = 5.4 - 6$ T with an "unfavorable" $\nabla \mathbf{B} \times \mathbf{B}$ direction, either by operating in upper single null (USN) configuration with the most common magnetic field direction, or by reversing the toroidal field and plasma current direction in lower single null (LSN) geometries. The plasma elongations were all relatively large $\kappa = 1.63 - 1.73$. The additional heating that is required for the formation of the temperature pedestal is provided by ion-cyclotron resonance heating (ICRH) with a maximum coupled power of 6 MW. (For more technical details on how the I-mode can be accessed, see, e.g., Ref. 19.)

The 2D fluctuation data are acquired by the gas-puff-imaging (GPI) system.[27] A poloidal section of Alcator C-Mod is shown in Fig. 1 with two arrays of GPI views overlaid. GPI records fluctuations of the intensity of the light emitted by a locally introduced diagnostic neutral gas. The emissivity is mostly dominated by electron impact excitation, which makes the observed brightnesses sensitive to a combination of T_e and n_e. The light intensity has been shown[28] locally to behave as a power function of both

$$I = A n_e^{\alpha_n} T_e^{\alpha_T}, \tag{1}$$

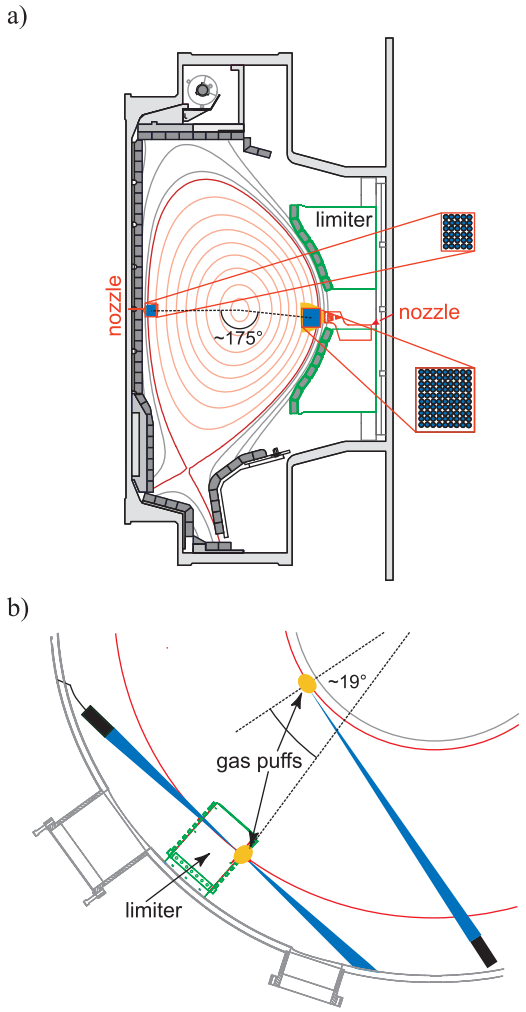

FIG. 1. Configuration of the GPI viewing arrays; (a) side view and (b) top view. The solid (red) D-shape curve represents the LCFS. Also marked are the toroidal and poloidal angles of separation between the two viewing arrays.

which for small fluctuations such as those observed in the plasma edge (typically $\delta n/n \lesssim 0.1$) gives us a normalized fluctuation level of

$$\frac{\tilde{I}}{I} = \alpha_n \frac{\tilde{n}_e}{n_e} + \alpha_T \frac{\tilde{T}_e}{T_e}. \quad (2)$$

In most C-Mod plasmas $\alpha_T \approx 0.0 - 0.1$, and even for the high temperatures and low densities of I-mode edge plasmas, one has an α_n at least a factor of 2, but mostly a factor 4–6 higher than α_T, so intensity fluctuations are normally considered as density fluctuations.[29]

On the low-field-side, the diagnostic gas puff enters from a nozzle mounted in the limiter, 2.54 cm below the height of the magnetic axis. The GPI viewing array covers a two-dimensional area of considerable size at this location, extending both into the region of closed flux surfaces and into that of open field lines. The viewing area is 3.5 cm (radial) × 3.9 cm (vertical), with an in-focus spot size of 3.8 mm for each of the 9 × 10 individual channels. On the high-field-side, the viewing array has the same resolution at approximately the height of the magnetic axis with a 6(horizontal)-by-5(vertical) array of views. All views are coupled to avalanche photodiodes (APD) sampled at 2 MHz. In order to enhance the gas-puff-enhanced-to-background brightness ratio, we used He puffs into D plasmas, therefore the recorded intensities are band-pass filtered for the HeI $(3^3D \rightarrow 2^3P)$, $\lambda = 587.6$ nm line. An example of the results of GPI density fluctuation measurements is shown in Fig. 2 from an I-mode as a conditional spectrum $S(k_\theta|f) = S(k,f)/S(f)$ exhibiting the known I-mode feature, the WCM.

Velocimetry is based on a time-delay-estimation (TDE) method that has been recently implemented for use on the fast 2D APD array. Cross-correlations are calculated directly from the observed brightness fluctuations on neighboring channels, thus the time lag τ_m of the maximum correlation can yield reasonable time histories for the local phase velocity of emissive structures as simply $v_\theta = \Delta z/\tau_m$. Due to the high sensitivity and low noise of the diagnostic, a time resolution of ~10 μs can be achieved, corresponding to a time lag estimated from samples as short as 20 frames. This 20 frame long sample pair is then moved forward frame by frame through the entire time history to provide velocimetry at every measurement point.

Owing to the fact that I-mode edge fluctuations exhibit a wave feature (the WCM) of—as yet—unknown origin, the time average component of the velocity spectrum from such a velocimetry algorithm cannot be accepted, since the phase velocity of emission features is a combination of true flow and wave propagation. For measurements of the mean $\mathbf{E} \times \mathbf{B}$ flow charge exchange spectroscopy (CXRS) was used,[30] where the local radial electric field was determined from B^{5+} populations according to

$$E_r = \frac{1}{Z_i n_i e} \partial_r p_i + v_{\phi,i} B_\theta - v_{\theta,i} B_\phi \quad (3)$$

in the (r, θ, ϕ) minor-radial, poloidal, toroidal coordinate system, where $Z_i = 5$ is the species charge and n_i, p_i, and $\mathbf{v}_i$ are its number density, pressure, and flow velocity, respectively.

III. MODE IDENTIFICATION

Until recently, Alcator C-Mod was one of the very few major tokamaks in the world on which GAM behavior had not been unambiguously observed.[31–34] Gas-puff-imaging of the large gradient region of the plasma edge in the I-mode operating regime has, however, provided poloidal velocity fluctuation spectra such as the one shown in Fig. 3. The spectra of the figure are averaged over the entire poloidal extent of the viewing array in order to improve the signal to noise ratio. The coherent peak around 20 kHz in Fig. 3 is, however, observable on individual pairs of channels as well. This facilitates an estimation of the poloidal mode number of the

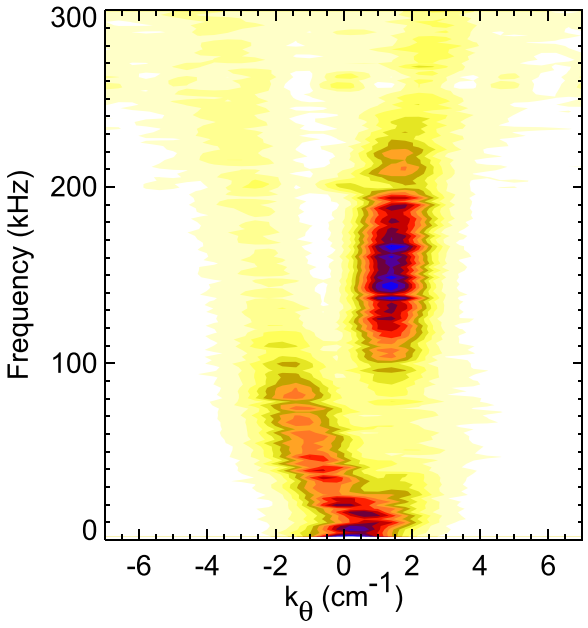

FIG. 2. Density fluctuations in the low-field-side edge of an I-mode plasma at $r/a = 0.95$; conditional wavenumber and frequency spectrum $S(k_\theta|f)$. The WCM appears as the broad feature at $f \approx 100$–200 kHz and $k_\theta = 1.3$ cm^{-1}, with a lab frame propagation in the electron diamagnetic drift direction.

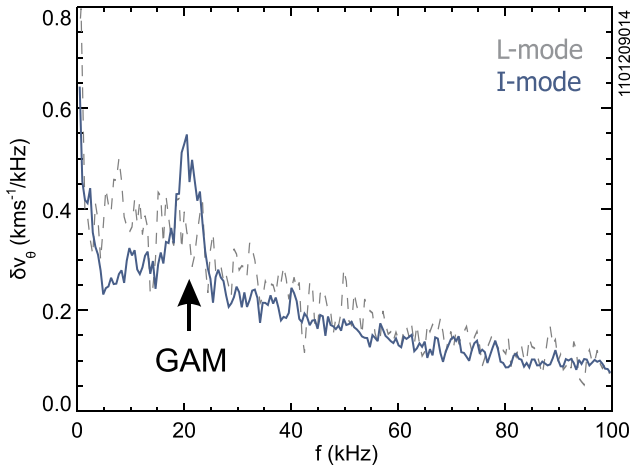

FIG. 3. Poloidally averaged Fourier spectra of TDE poloidal velocities in an I-mode (solid blue) and the preceding L-mode (dashed grey). The sample size for correlation measurements is $n_{cor} = 20$, the spectra are time averaged from a spectrogram with $df = 0.5$ kHz.

mode structure, which is a crucial step in identifying the feature as a fluctuating zonal flow, i.e., a GAM.

In recent experiments, both the low-field-side GPI array[27] and the new APD-coupled views of the high-field-side (see Fig. 1) were utilized for similar measurements. Since the two viewing locations are barely separated toroidally ($\Delta\phi \approx 19^\circ$), the phase delay between the two locations provides information on the large scale poloidal structure ("m" mode number). The velocity oscillations at the two poloidal locations and at the frequency range in question were shown to be *in phase* with an error of $\delta\varphi(in, out) \approx 0.05$ estimated from the average deviation of the phase within the spectral width of the mode. Since the poloidal separation between the two regions is $\Delta\theta = 175^\circ$, this result restricts the poloidal mode number to even values. In addition, an upper bound can be placed on m by comparing the spectra at the two ends of the poloidal span of the outboard viewing array. Figure 4 demonstrates a high level of coherency between the inboard and outboard views as well as the top and bottom of the outboard viewing array. With the error bar on the measured phase calculated as before, one then has an upper bound on m according to

$$m^{\max} = k_z^{\max} a = \frac{\delta\varphi a}{\Delta z}. \tag{4}$$

With the values from the graph, the poloidal mode number can be said to be $m \lesssim 2$, with the error bar just below the limit for $m = 2$. Thus, since the mode number must be both even and less than 2, the structure can be safely regarded poloidally symmetric.

Finally, the oscillations are validated as geodesic-acoustic modes by comparing the frequencies measured from spectra such as the one in Fig. 3 with the theoretical expectation[11] based on a combination of local electron cyclotron emission (ECE) and Thomson scattering[35] measurements of electron temperature. The error bars in Fig. 5 are traced from the estimated errors of the temperature measurement (up to ~100–150 eV)[21] in c_s and the full width at half maximum in f_{GAM}. Note that the sound speed is estimated *without* the effective atomic number Z_{eff}, as $c_s = (2T_e/m_i)^{1/2}$; the measured values nevertheless line up reasonably well with previous observations from other tokamak devices (reproduced from Ref. 36) and the simplified theoretical expectation $\omega_{\mathrm{GAM}} = c_s/R$ for a circular cross-section. Note that the measured frequencies fall below this basic prediction in accordance with the strong inverse scaling against elongation κ demonstrated in several experiments.[3,37,38] Empirical scalings of GAM frequencies observed in C-Mod, however, fall outside of the scope of this paper.

IV. SPATIAL STRUCTURE AND E × B SHEAR

As described above, in the process of validating the identification of the coherent poloidal velocity fluctuation as GAM, the poloidal part of the mode's spatial structure was shown to be $m = 0$. Its radial location and phase relations are, however, relevant also to the detailed physical picture of the I-mode. In particular, the edge plasmas of the C-Mod I-mode are known to exhibit a weakly coherent mode (WCM)[19] as well as a mean shear flow,[26] mostly known in this context as a "radial electric field well" (E_r-well). The two features have been shown to exist at approximately the same radial position. The new measurements of both velocity and density fluctuations reported here corroborate this general result. Indeed as demonstrated in Fig. 6, they place also

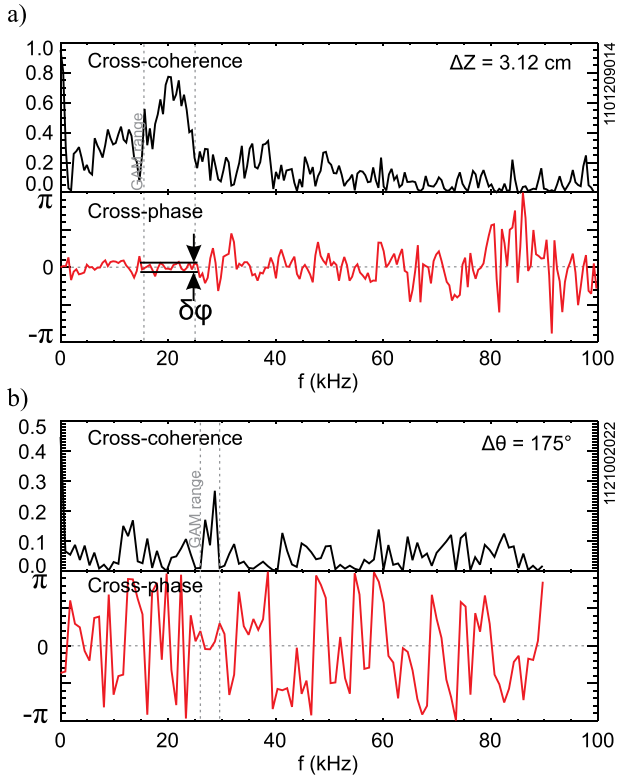

FIG. 4. Cross-coherency and cross-phase (a) between the top and bottom TDE view-pairs on the outboard side GPI array and (b) between the inboard and outboard GPI arrays. The latter are conditionally averaged for the times at which the fluctuation level is sufficiently large for the TDE routine to reliably lock into propagating features.

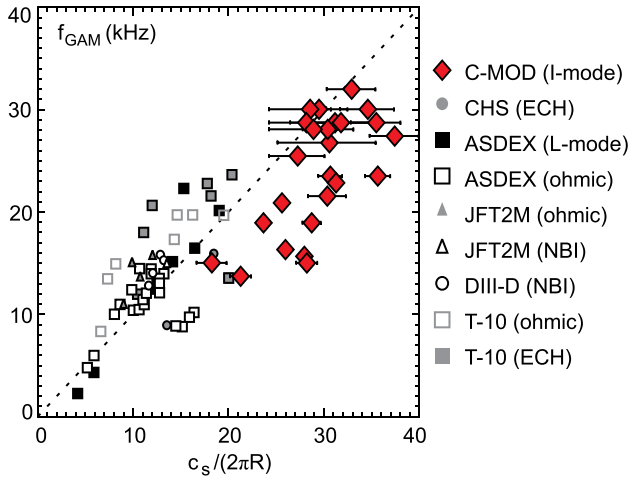

FIG. 5. GAM frequencies against the theoretical c_s/R from a large number of experiments, with the recent results from Alcator C-Mod overlaid as the red squares. The dashed line represents $\omega = c_s/R$. Original reprinted with permission from A. Fujisawa *et al.*, Nucl. Fusion **47**, S718 (2007). Copyright (2007) International Atomic Energy Agency.

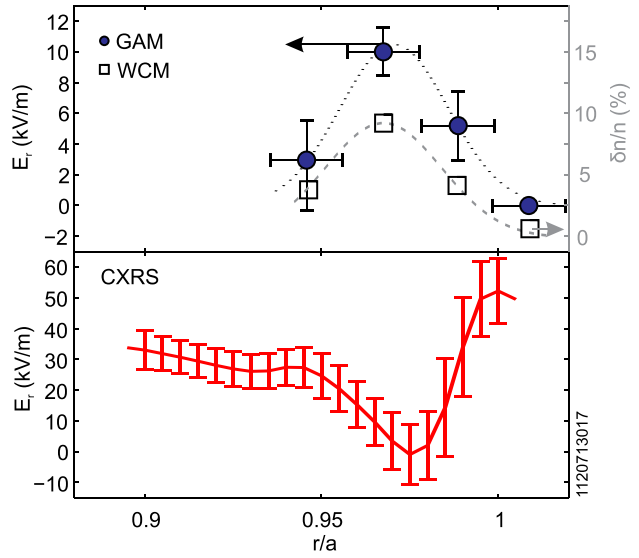

FIG. 6. Radial location of the edge turbulence features in I-mode; (top) radial profile of the mode amplitude of the WCM (squares, right axis) and the GAM (full circles, left axis) exhibiting nearly identical distributions; (bottom) radial electric field profile in the same I-mode discharge as above in a sample including the time of the velocity measurement. Profile is calculated from CXRS measurements.

the GAM activity to where the mean E_r well is detected via CXRS.

This observation has three important implications: (1) the fluctuations of the poloidal flow velocity have a non-zero mean flow background, (2) the poloidal speed of the WCM at its maximum can be measured in the frame co-moving with the average $\mathbf{E} \times \mathbf{B}$ flow, and (3) the shared spatial location of the GAM and WCM open up the question of temporal characteristics and mode interaction in this increasingly complicated picture of edge turbulence.

The first one of these can be approached from the opposite perspective as well, namely, that it is the edge zonal flow that is fluctuating. While the latter phrasing corresponds well to the theoretical expectation of the collisionless GAM damping which leaves behind the Rosenbluth–Hinton residual, i.e., the zonal flow,[1,10,39] it also highlights the need for a quantitative comparison between the two flows. The sample that is analyzed for both steady state electric field and GAM profiles in Fig. 6 was taken from a steady I-mode, with a well-developed temperature pedestal and E_r-well, both of which lie in the mid-range of values observed during C-Mod I-mode discharges.[21] It is worth mentioning here that the background flow and the turbulence driven component of this electric field are experimentally indistinguishable. The graphed GAM profile (mode amplitude, i.e., 1/2 peak-to-peak) shows a typical magnitude in the velocity fluctuation of $\tilde{v}_\theta = 2.2\,\mathrm{km/s}$ corresponding to $\tilde{E}_r = 10\,\mathrm{kV/m}$, while the depth of the time-average well is approximately $\bar{E}_r = 30\,\mathrm{kV/m}$. Due to the considerable amount of noise in the detection of velocities from the motion of turbulent structures, the empirical GAM amplitude must be regarded as a lower estimate. Even so *the slowly evolving edge flow (including ZF) velocity and the GAM amplitude velocity are of comparable magnitude* and, therefore, the radial shear is at least partially *periodically destroyed* in an I-mode.

For the second point, we here note that we are considering the "central" frequency of the WCM, the meaning of which will be elucidated in Sec. V. For now, we simply take it as the centroid of the frequency range at which the WCM appears in the shot plotted in Fig. 6, $f_{\mathrm{WCM}} = 200\,\mathrm{kHz}$. This leads to a propagation speed in the frame moving with the local $\mathbf{E} \times \mathbf{B}$ velocity at $v_\theta = 12.1 \pm 3.8\,\mathrm{km/s}$ in the electron diamagnetic drift direction (including an error of only 20 kHz in the frequency, see Sec. V). The speed is still considerably smaller than the electron diamagnetic velocity at $v_e^* = 31 \pm 10\,\mathrm{km/s}$.

Finally, Fig. 7 shows the spectrograms of poloidal velocity and density fluctuations in a typical I-mode onset followed by a long, steady I-mode, which lasts longer than the 0.3 s duration of the GPI data window. In the given example, the L-I transition settles at 1.13 s, marked by the change of slope in the decay of the edge electron temperature following the arrival of the heat-pulse due to the sawtooth crash shown in the top two panels of the figure. The two "dithers" into I-mode before this time are rather common at the onset of the regime, their "on"-phase always triggered by the temperature increase at the arrival of sawtooth heat-pulses.[40] As previously reported, the WCM is completely contemporaneous with the I-mode. It is important to note, however, that the WCM only appears as the distinguishable, broad feature at high frequencies, when the GAM (apparent as the narrow peak in the middle panel) is present. The GAM appears sensitive to local T_e, as a drop of $\sim 100\,\mathrm{eV}$ ($\sim 20\%$) during the sawtooth cycle in this transient stage is enough to eliminate it, while in the case of the WCM, it is the lab frame frequency of the mode that is clearly modulated by the temperature fluctuations, perhaps indicating a Doppler-shift by a temporary increase of the diamagnetic component of E_r. Nevertheless, the most obvious feature of the experiment is that in the I-mode the GAM is not a transient mode that quickly dissipates and leaves behind the residual Rosenbluth–Hinton-flow to saturate turbulence, but it exists

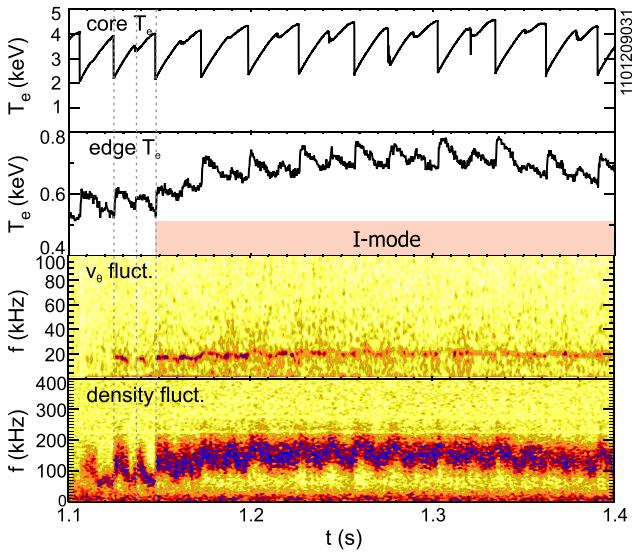

FIG. 7. Time history of a long lived I-mode discharge; (a) core electron temperature, (b) electron temperature at the GAM measurement location, i.e., the top of the pedestal, (c) spectrogram of the TDE poloidal velocity $\tilde{v}_\theta$, (d) spectrogram of density fluctuations $\tilde{n}$ in the same spatial location restricted to a wavenumber range $0.5\,\mathrm{cm}^{-1} < k_\theta < 2.0\,\mathrm{cm}^{-1}$ to highlight the WCM. (a) and (b) are measured via ECE and (c) and (d) by GPI.

through the entire duration of the I-mode along with the mean shear flow, which can be as large as 100 kV/m in some cases.

V. MODE INTERACTIONS

The typical onset of the I-mode regime indicates that there is a significant interplay between GAM and WCM fluctuations. This section examines the fine details of this phenomenon. The conditional wavenumber-frequency spectrum $S(k|f)$ of the edge density fluctuations, shown in Fig. 2, reveals that the WCM, even though it is quite broad in the frequency space,[19,20] occupies quite a narrow band in wavenumber space at $k_\theta = 1.3 \pm 0.5\,\mathrm{cm}^{-1}$. This is consistent with the effect of a velocity field fluctuating in the poloidal direction.

The lowest order of the spectral transfer process can be quantified in terms of bispectral estimates, which describe three-wave coupling. Here, we take a two-field approach to the turbulence fluctuation dynamics similar to that employed for GAM convection studies in Ref. 41 and for spectral transfer in the frequency space in Ref. 42; namely, we proceed from the continuity equation

$$\partial_t n + \mathbf{v} \cdot \nabla n = -n \nabla \cdot \mathbf{v}, \tag{5}$$

in which we arranged the terms this way because the compressibility term on the right-hand-side is a linear, dissipative coupling between the two fluctuation fields (density and—in our case—velocity) of the turbulence, while the first two terms correspond to the local apparent rate of change and the turbulent convection. In order to elucidate the spectral transfer characteristics of these terms, we reformulate (5) as a Fourier series

$$\tilde{n}_f^* \partial_t \tilde{n}_f + \tilde{n}_f^* v_{f_2}^i \partial_i \tilde{n}_{f_1} = -\tilde{n}_f^* \mathcal{K}, \tag{6}$$

where the second term represents three-wave coupling, $\mathcal{K}$ stands for the compressibility term, regardless of its exact form, and due to orthogonality, the multiplication by the complex conjugate of each component $\tilde{n}_f^*$ separates the equation series into mode-by-mode equations and enforces the constraint $f = f_1 + f_2$. The partial time derivative in (6) stands for a slow time parameter against which the history of the local turbulence power can be examined. Thus,

$$\frac{1}{2}\partial_t \langle |\tilde{n}_f|^2 \rangle = -\Re \langle \tilde{n}_f^* \tilde{v}_{f-f_1}^i \partial_i \tilde{n}_{f_1} \rangle - \Re \langle \tilde{n}_f^* \mathcal{K} \rangle. \tag{7}$$

The first term on the right hand side still includes the time average components as a "zero-frequency" term: $\langle \tilde{n}_f^* \tilde{v}_f^i \rangle \partial_i n_0$ where the dominant term is $\partial_r n_0$ since the density varies little poloidally compared to the background radial gradient, and the term shows how the turbulence can extract power from this gradient via the mass flux. Then in a simplified form, we can write the wave kinetic equation as

$$\partial_t P_n(f) = -\gamma_n(f) P_n(f) + \sum_{f_1} T_n(f_1, f), \tag{8}$$

where γ_n now contains all linear driving and damping be it from any mechanism, while the spectral transfer term is identified as $T_n(f_1,f) = -\Re \langle \tilde{n}_f^* \tilde{v}_{f-f_1}^i \partial_i \tilde{n}_{f_1} \rangle$, where f_1 corresponding to density gradient fluctuations and f to density fluctuations. With this sign convention, (8) makes it clear that if $T_n(f_1,f)$ is positive (negative), the components at "target" frequency f are gaining (losing) power and the components at the "source" frequency f_1 are losing (gaining) it via the convection represented in the $\tilde{v}_{f-f_1}^i$ term. Since we are concentrating on the effects of the GAM, a poloidal velocity fluctuation, the nonlinear transfer term under more scrutiny is $T_n^\theta(f_1,f) = -\Re \langle \tilde{n}_f^* \tilde{v}_{f-f_1}^\theta \frac{1}{r} \partial_\theta \tilde{n}_{f_1} \rangle$.

Figure 8 shows an example of the results of such a measurement. The terms in the transfer function here are measured as follows. Velocity measurements are available from adjacent, poloidally separated pairs of views, where the density fluctuation spectra are $\tilde{n}_f^1$ and $\tilde{n}_f^2$. This pair of views is then one point of measurement, where

$$\begin{aligned} \tilde{n}_f &= \frac{\tilde{n}_f^1 + \tilde{n}_f^2}{2}, \\ \tilde{v}_f^\theta &= \mathcal{F}\left(\frac{\Delta z}{\tau_m}\right), \\ \frac{1}{r}\partial_\theta \tilde{n}_f &= \frac{\tilde{n}_f^2 - \tilde{n}_f^1}{\Delta z}, \end{aligned} \tag{9}$$

where $\mathcal{F}$ represents a Fourier-transform. The expression is evaluated for each pair of poloidally adjacent points and is then both time averaged for a suitably chosen, stationary segment and poloidally averaged. Further, since our expression for T_n is inherently anti-symmetric[41] for a change of the variables f_1 and f, the spectrum in Fig. 8 was first integrated along fixed values of $f - f_1$ to see if the spectra are quantitatively conforming to this constraint. Once this was confirmed, T_n was further antisymmetrized to remove any noise arising from the relatively short samples (the figure shown was averaged over ~200 realizations per location) and background noise, that is, we plot $T_n^A(f_1,f) = (T_n(f_1,f) - T_n(f,f_1))/2$.

The main feature in Fig. 8(a) of the bispectrum is two lobes at $f = f_1 \pm 20\,\mathrm{kHz}$. The negative values at $f = f_1 + 20\,\mathrm{kHz}$ up to about $f_1 = 150\,\mathrm{kHz}$ mean that the density fluctuations one GAM frequency $f_{\mathrm{GAM}} = 20\,\mathrm{kHz}$ higher than the density-gradient fluctuations are losing power to the latter. Conversely, though, the positive values at $f = f_1 - 20\,\mathrm{kHz}$ mean that the density fluctuations one GAM frequency *smaller* than the density gradient fluctuations are gaining this power back. In other words, the coupling to the GAM in the WCM causes the density fluctuation power to move down to lower frequencies in steps of the GAM frequency.

In order to highlight the frequency ranges in which the transfer produces the most significant portion of the spectrum, the bispectrum can be normalized to the density fluctuation spectrum. Figure 8(c) graphs the normalized spectrum $T_n(f_1,f)/(|\tilde{n}(f_1)|^2 |\tilde{n}(f)|^2)^{1/2}$, which reveals an essential new feature. The two lobes we noted in part a) of the figure are indeed the dominant peaks in the spectrum, but they are now shown to extend up to about 230 kHz, or as $S(k_\theta|f)$ of Fig. 2 shows, the entire range of the WCM. In addition, they

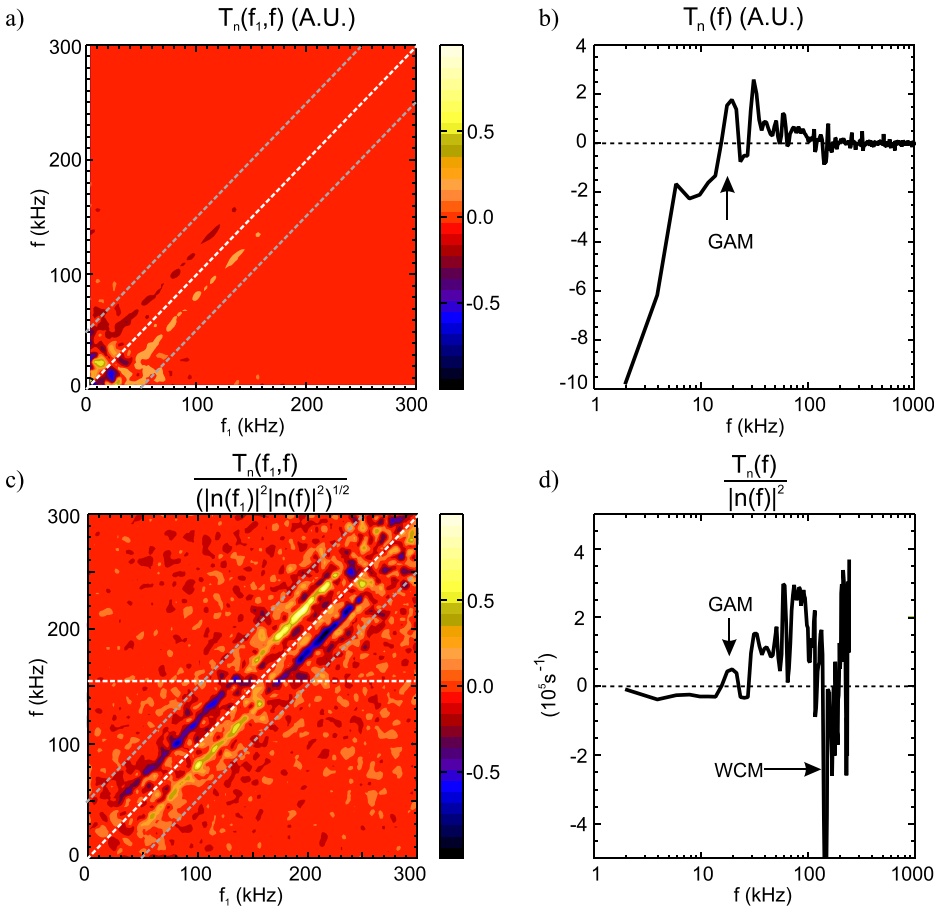

FIG. 8. Nonlinear spectral transfer of density fluctuation power; (a) nonlinear transfer $T_n^\theta(f_1,f)$ as a function of source frequency f_1 and target frequency f, with a $f_1 = f$ overlaid as the white dashed line, and the boundaries of meaningful velocity measurements marked by dashed grey lines; (b) transfer function $T_n^\theta(f)$, with a clear positive peak at f_{GAM}; (c) nonlinear transfer normalized to the spectral power of source and target components, with the horizontal dashed line marking the central frequency of the WCM; (d) effective transfer rate, i.e., transfer function normalized to the spectral power with a clear negative peak at the WCM frequency marked in plot (c). High frequency noise is clipped at $f = 250$ kHz in part (d).

change sign just at the "central" WCM frequency, indicating that fluctuation power is in fact transferred away from this relatively narrow $\Delta f = 20$ kHz band towards both lower and higher frequencies.

Integration of the bispectrum over f_1 gives us a picture of the net gain of a frequency component in the spectra via the studied three-wave process. Figures 8(b) and 8(d) are the transfer functions integrated along lines parallel to the horizontal dashed white line in part c). The broad-band, low frequency segment of the density spectrum exhibits loss of power in a process leading to a GAM gain. It is also clear that the central frequency of the WCM loses power in favor of the broad frequency range around it, therefore there must be an underlying wave instability, which causes an actually fairly coherent $\Delta f/f = 0.1$ source to appear in the plasma frame.

VI. DRIVE AND DAMPING

Using cross-bispectra similar to the one analyzed in Sec. V, one can directly measure the transfer of kinetic energy into (an out of) the GAM and potentially the ZF as well. As before, we define the kinetic energy transfer term $T_v(f_1,f)$ as

$$T_v(f_1,f) = -\Re\langle \tilde{v}_f^\theta \tilde{v}_{f-f_1}^r \partial_r \tilde{v}_{f_1}^\theta \rangle, \tag{10}$$

where the above term remains from the complete form of $\langle \tilde{v}_f^j \tilde{v}_{f-f_1}^i \partial_i \tilde{v}_{f_1}^j \rangle$ because we are interested in the poloidal flow and, as Sec. III described, $\partial_\theta \tilde{v}^\theta = 0$ to a very good approximation. For more details about the kinetic energy transfer function analysis, see Refs. 42–45. Normalization of the integral transfer function to the kinetic energy spectrum in this case provides an effective nonlinear growth rate of the energy contained in the mode,

$$\gamma_{\mathrm{NL}} = \frac{\sum_{f_1} T_v(f_1,f)}{|v_\perp|^2(f)}. \tag{11}$$

As the low-frequency segment in Fig. 8, here the entire broad-band spectrum (5–15 kHz and 25–100 kHz) exhibits a net kinetic energy loss. These results are qualitatively similar to previous observations by various diagnostics of the reduction of turbulence below the frequency range of the WCM at the onset of the I-mode.[20,21] At the same time, it is interesting to notice the most evident difference between Figs. 8(d) and 9(b). In the spectrum of the kinetic energy transfer rate, the very lowest frequency components exhibit a large positive value, while there is no such peak in the case of the density fluctuation transfer rate. This could indicate that even though the time average velocity (0th Fourier-component) of the velocity spectra cannot be trusted as reliable, we do still observe the Rosenbluth–Hinton-modes due to their finite frequency width, since unlike in the case of the GAM, no density component is expected in these modes while the kinetic energy of the turbulence is definitely piling up in the ZF. The growth rate at the GAM frequency in Figure 9(b) is $\gamma_{\mathrm{NL}}^{\mathrm{GAM}} = 3.5 \times 10^4\ \mathrm{s}^{-1}$, which is, remarkably, almost exactly the same as the rate measured from density bispectra above.

To compare this growth rate to the theoretically expected damping, we first note that since the rate of GAM

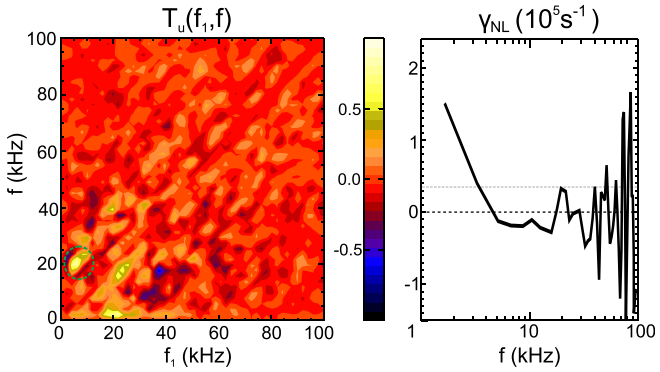

FIG. 9. Nonlinear kinetic energy transfer function $T_u(f_1,f)$ (left) and the effective nonlinear growth rate $\gamma_{NL} = (\sum_{f1} T_u(f_1,f))/|v|^2(f)$.

Landau damping[12] carries an explicit $\exp(-q^2)$ factor, this damping mechanism is negligible at the high safety factor of $q \approx 4$ used here. The collisional damping rate is predicted neoclassically[13] to be $\gamma = 4/7(\nu_{ii}/q)$, which is $\gamma \approx 1.5 \times 10^4\,s^{-1}$ for the conditions during the analysis period and is of comparable magnitude to the value obtained in bispectral analysis.

Given that both the drive and the damping rates can be calculated from directly measured quantities, it makes sense to ask the question how these evolve at the L-I and I-H transitions, and in particular to determine if the transfer rate exceeds the damping rate during such transitions (as would be expected if this physics plays a role in the transition into or out of I-mode). For this purpose, a shot was chosen with a typical I-mode onset such as the one in Fig. 7, but one with a subsequent transition into H-mode. Even though the bispectra take a large number of realizations to thoroughly converge, we may estimate the nonlinear growth rate in a time resolved sense as follows. In the first part of Fig. 9, one can identify the frequency range in the (f_1,f) space that gives the largest positive contribution to the GAM growth. In this process, we need to concentrate only on the off-diagonal terms, since unlike the density cross-bispectrum, the kinetic energy transfer function was *not* defined inherently anti-symmetrically, and the diagonal terms do not represent energy transfer (source and target are the same). In the figure, a green dashed circle indicates this region, and in Fig. 10, the velocity components were digitally filtered to match the parameters of the bright peak in the spectrum. In addition the time-resolved growth rate curve was box-car averaged to the period of the slowest component of the triple product of velocity fluctuations at 5 kHz.

Even though the above is a crude estimate of what the real nonlinear driving term might be, the results in Fig. 10 are quite remarkable. As the temperature at the location where the GAM will appear grows, the collisional damping rate slowly decreases, since $\nu_{ii} \propto T_i^{-3/2}$, while the increased temperature gradient drives more and more turbulence, which can now nonlinearly drive a GAM. At the time when the drive becomes stronger than the damping, the GAM appears in the velocity spectrum. As the temperature drops towards the end of the sawtooth cycle, the damping grows larger than the drive once again, and the GAM drops out, along with the WCM. After the analysis in Sec. V, it is worth drawing attention to the fact that the WCM does not completely disappear, but a narrow

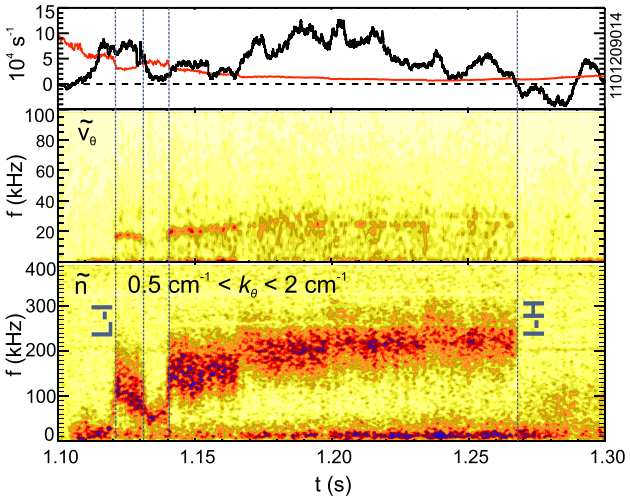

FIG. 10. Time history of a typical L-I transition followed by an I-H transition event; graphs are from top to bottom: the solid black line represents the estimated, time-resolved, non-linear GAM drive $\tilde{\gamma}_{NL}$, the red curve corresponds to $4\nu_{ii}/7q$ estimated from ECE and Thompson scattering, the middle panel shows $|\tilde{v}_\theta|(f,t)$, and the bottom $|\tilde{n}|^2(f,t|k \in [0.5,2.0])$.

mode at very small frequency remains in lieu of the GAM. It is also interesting to observe the behavior of the GAM at the I-H transition. As the temperature increases in the edge at every sawtooth crash, the WCM is shifted to higher and higher frequencies, presumably the result of increased mean flow appearing in the Doppler shifted frequencies. CXRS measurements are not available at this time resolution, but it is reasonable to speculate that the growing temperature gradient supports a larger and larger mean shear flow. Parallel to this, the GAM drive is becoming weaker, as—presumably—the branching ratio is now shifting towards the ZF. Just before the I-H transition, the GAM drive disappears, likely because the turbulence that feeds the GAM is now sheared away.

VII. SUMMARY

Using fast 2D gas-puff-imaging, a coherent poloidal velocity fluctuation was found in the edge of I-mode plasmas. The spatial structure, with a poloidal mode number of $m = 0$, the velocity primarily in the poloidal direction, corresponding to a fluctuating E_r and the scaling of the mode frequency with the local temperature as $f \propto T_e^{1/2}$ are all consistent with the identification of the feature as a geodesic-acoustic mode. While no other confinement regimes reproducibly and unambiguously exhibit GAM behavior on Alcator C-Mod, all I-modes tested so far have shown a continuous presence of these modes. Since the I-mode also features a strong (20–100 kV/m) mean E_r-well, it is a regime in which a mean shear flow (including ZF) and GAM continuously coexist, and an evolution of the branching ratio is observed in transitions of the confinement regime.[46]

The GAM is contemporaneous with the I-mode specific WCM responding sensitively to the changes of local temperature, especially at the onset of the I-mode confinement regime. Cross-bispectral measurements of the spectral transfer of density fluctuations showed that the GAM is responsible for the broad frequency structure of the WCM, while being driven by the broadband turbulence. Measurement of the nonlinear kinetic energy transfer allowed an estimation of the effective

growth rate of this nonlinear drive, yielding an approximate $\gamma_{NL} = 3.5 \times 10^4\ s^{-1}$.

Time resolved estimates of the same process made it possible to compare the evolution of edge collisional GAM damping rates to its drive. I-mode is initiated when GAM are accessible. I-mode ends when GAM are either damped out by collisions (cold edge, transition into L-mode), *or* when the mean velocity shear becomes more efficient at reducing turbulence (quiescent edge, transition into H-mode). Both this and the identification of the GAM as the source of the weak coherence in the WCM suggest that the GAM could be a key player in the dynamics of the I-mode. To support this speculation, we note that the recently reported scalings of the threshold auxiliary power needed to initiate I-modes[21] are remarkably similar to what would be expected if the GAM was the trigger to I-mode: $P_{th} \propto n_e$ for a fixed geometry, similarly to the damping $\gamma \propto \nu_{ii} \propto n_i$, and $P_{th} \propto I_p$ for a restricted range of toroidal fields and densities, perhaps corresponding to $\gamma \propto q^{-1} \propto I_p$. Further studies involving a large number of I-modes for threshold scalings based on the drive–damping-comparison will be necessary to show this role, as well as studies regarding the modulation of heat and mass flux across the magnetic field and the possible connection to the separation of these transport channels.

ACKNOWLEDGMENTS

The authors would like to thank Martin Greenwald, Earl Marmar, and Anne White for the discussions and the insightful comments as well as the Alcator C-Mod team of students, scientists, engineers, and technical staff for making the experiments possible. This work was supported by U.S. Department of Energy Cooperative Agreement No. DE-FC02-99ER54512.

[1]P. H. Diamond, S. Itoh, K. Itoh, and T. S. Hahm, Plasma Phys. Controlled Fusion **47**, R35 (2005).
[2]G. R. Tynan, A. Fujisawa, and G. McKee, Plasma Phys. Controlled Fusion **51**, 113001 (2009).
[3]A. Fujisawa, Nucl. Fusion **49**, 013001 (2009).
[4]B. A. Carreras, IEEE Trans. Plasma Sci. **25**, 1281 (1997).
[5]W. Horton, Rev. Mod. Phys. **71**, 735 (1999).
[6]P. W. Terry, Rev. Mod. Phys. **72**, 109 (2000).
[7]C. Holland, P. H. Diamond, S. Champeaux, E. J. Kim, O. Gürcan, M. N. Rosenbluth, G. R. Tynan, N. Crocker, W. M. Nevins, and J. Candy, Nucl. Fusion **43**, 761 (2003).
[8]P. H. Diamond, S. Champeaux, M. Malkov, A. Das, I. Gruzinov, M. N. Rosenbluth, C. Holland, B. Wecht, A. I. Smolyakov, F. L. Hinton, Z. Lin, and T. S. Hahm, Nucl. Fusion **41**, 1067 (2001).
[9]N. Chakrabarti, R. Singh, P. K. Kaw, and P. N. Guzdar, Phys. Plasmas **14**, 052308 (2007).
[10]M. N. Rosenbluth and F. L. Hinton, Phys. Rev. Lett. **80**, 724 (1998).
[11]N. Winsor, J. L. Johnson, and J. M. Dawson, Phys. Fluids **11**, 2448 (1968).
[12]V. B. Lebedev, P. N. Yushmanov, P. H. Diamond, S. V. Novakovskii, and A. I. Smolyakov, Phys. Plasmas **3**, 3023 (1996).
[13]S. V. Novakovskii, C. S. Liu, R. Z. Sagdeev, and M. N. Rosenbluth, Phys. Plasmas **4**, 12 (1997).
[14]J. C. Hillesheim, W. A. Peebles, T. A. Carter, L. Schmitz, and T. L. Rhodes, Phys. Plasmas **19**, 022301 (2012).
[15]P. Manz, G. S. Xu, B. N. Wan, H. Q. Wang, H. Y. Guo, I. Cziegler, N. Fedorczak, C. Holland, S. H. Müller, S. C. Thakur, M. Xu, K. Miki, P. H. Diamond, and G. R. Tynan, Phys. Plasmas **19**, 072311 (2012).
[16]G. D. Conway, C. Angioni, F. Ryter, P. Sauter, J. Vicente, and ASDEX Upgrade Team, Phys. Rev. Lett. **106**, 065001 (2011).
[17]L. Schmitz, L. Zeng, T. L. Rhodes, J. C. Hillesheim, E. J. Doyle, R. J. Groebner, W. A. Peebles, K. H. Burrell, and G. Wang, Phys. Rev. Lett. **108**, 155002 (2012).
[18]F. Ryter, W. Suttrop, B. Brüsehaber, M. Kaufmann, V. Mertens, H. Murmann, A. G. Peeters, J. Stober, J. Schweinzer, H. Zohm, and ASDEX Upgrade Team, Plasma Phys. Controlled Fusion **40**, 725 (1998).
[19]D. G. Whyte, A. E. Hubbard, J. W. Hughes, B. Lipschultz, J. E. Rice, E. S. Marmar, M. Greenwald, I. Cziegler, A. Dominguez, T. Golfinopoulos *et al.*, Nucl. Fusion **50**, 105005 (2010).
[20]A. E. Hubbard, D. G. Whyte, R. M. Churchill, I. Cziegler, A. Dominguez, T. Golfinopoulos, J. W. Hughes, J. E. Rice, I. Bespamyatnov, M. J. Greenwald *et al.*, Phys. Plasmas **18**, 056115 (2011).
[21]A. E. Hubbard, D. G. Whyte, R. M. Churchill, A. Dominguez, J. W. Hughes, Y. Ma, E. S. Marmar, Y. Lin, M. L. Reinke, and A. E. White, Nucl. Fusion **52**, 114009 (2012).
[22]F. Wagner, G. Becker, K. Behringer, D. Campbell, A. Eberhagen, W. Engelhardt, G. Fussmann, O. Gehre, J. Gernhardt, G. v. Gierke *et al.*, Phys. Rev. Lett. **49**, 1408 (1982).
[23]M. Greenwald, R. L. Boivin, F. Bombarda, P. T. Bonoli, C. L. Fiore, D. Garnier, J. A. Goetz, S. N. Golovato, M. A. Graf, R. S. Granetz *et al.*, Nucl. Fusion **37**, 793 (1997).
[24]R. J. Groebner and T. N. Carlstrom, Plasma Phys. Controlled Fusion **40**, 673 (1998); T. N. Carlstrom, K. H. Burrell, and R. J. Groebner, *ibid.* **40**, 669 (1998).
[25]I. H. Hutchinson, R. Boivin, F. Bombarda, P. Bonoli, S. Fairfax, C. Fiore, J. Goetz, S. Golovato, R. Granetz, M. Greenwald *et al.*, Phys. Plasmas **1**, 1511 (1994).
[26]R. M. McDermott, B. Lipschultz, J. W. Hughes, P. J. Catto, A. E. Hubbard, I. H. Hutchinson, R. S. Granetz, M. Greenwald, B. LaBombard, K. Marr, M. L. Reinke, J. E. Rice, D. Whyte, and Alcator C-Mod Team, Phys. Plasmas **16**, 056103 (2009).
[27]I. Cziegler, J. L. Terry, J. W. Hughes, and B. LaBombard, Phys. Plasmas **17**, 056120 (2010).
[28]D. P. Stotler, J. Nucl. Mater. **313–316**, 1066 (2003).
[29]I. Cziegler, Ph.D. dissertation, Massachusetts Institute of Technology, Cambridge, 2011.
[30]C. Theiler, R. M. Churchill, B. Lipschultz, T. Pütterich, A. Diallo, A. Hubbard, J. W. Hughes, E. Marmar, M. L. Reinke, J. L. Terry, J. R. Walk, and D. Whyte, Bull. Am. Phys. Soc. **57**, 12 (2012).
[31]G. R. McKee, R. J. Fonck, M. Jakubowski, K. H. Burrell, K. Hallatschek, R. A. Moyer, D. L. Rudakov, W. Nevins, G. D. Porter, P. Schoch, and X. Xu, Phys. Plasmas **10**, 1712 (2003).
[32]G. D. Conway, B. Scott, J. Schirmer, M. Reich, A. Kendl, and ASDEX Upgrade Team, Plasma Phys. Controlled Fusion **47**, 1165 (2005).
[33]K. J. Zhao, T. Lan, J. Q. Dong, L. W. Yan, W. Y. Hong, C. X. Yu, A. D. Liu, J. Qian, J. Cheng, D. L. Yu, Q. W. Yang, X. T. Ding, Y. Liu, and C. H. Pan, Phys. Rev. Lett. **96**, 255004 (2006).
[34]T. Ido, Y. Miura, K. Hoshino, K. Kamiya, Y. Hamada, A. Nishizawa, Y. Kawasumi, H. Ogawa, Y. Nagashima, K. Shinohara, Y. Kusama, and JFT-2M Group, Nucl. Fusion **46**, 512 (2006).
[35]J. W. Hughes, D. A. Mossessian, A. E. Hubbard, and E. S. Marmar, Rev. Sci. Instrum. **72**, 1107 (2001).
[36]A. Fujisawa, T. Ido, A. Shimizu, S. Okamura, K. Matsuoka, H. Iguchi, Y. Hamada, H. Nakano, S. Ohshima, K. Itoh *et al.*, Nucl. Fusion **47**, S718–S726 (2007).
[37]G. R. McKee, D. K. Gupta, R. J. Fonck, D. J. Schlossberg, M. W. Shafer, and P. Gohil, Plasma Phys. Controlled Fusion **48**, S123–S136 (2006).
[38]G. D. Conway and ASDEX Upgrade Team, Plasma Phys. Controlled Fusion **50**, 085005 (2008).
[39]F. L. Hinton and M. N. Rosenbluth, Plasma Phys. Controlled Fusion **41**, A653–A662, (1999).
[40]Y. R. Martin and TCV Team, Plasma Phys. Controlled Fusion **46**, A77–A85 (2004).
[41]C. Holland, G. R. Tynan, R. J. Fonck, G. R. McKee, J. Candy, and R. E. Waltz, Phys. Plasmas **14**, 056112 (2007).
[42]M. Xu, G. R. Tynan, C. Holland, Z. Yan, S. H. Muller, and J. H. Yu, Phys. Plasmas **16**, 042312 (2009).
[43]P. Manz, M. Ramisch, and U. Stroth, Phys. Rev. Lett. **103**, 165004 (2009).
[44]P. Manz, M. Xu, N. Fedorczak, S. C. Thakur, and G. R. Tynan, Phys. Plasmas **19**, 012309 (2012).
[45]M. Xu, G. R. Tynan, P. H. Diamond, P. Manz, C. Holland, N. Fedorczak, S. C. Thakur, J. H. Yu, K. J. Zhao, J. Q. Dong *et al.*, Phys. Rev. Lett. **108**, 245001 (2012).
[46]K. Miki and P. H. Diamond, Nucl. Fusion **51**, 103003 (2011).